

Fluorescence molecular optomic signatures improve identification of tumors in head and neck specimens

Yao Chen¹, Samuel S. Streeter¹, Brady Hunt^{1,6}, Hira S. Sardar¹, Jason R. Gunn¹, Laura J. Tafe^{2,4}, Joseph A. Paydarfar^{2,3,5}, Brian W. Pogue^{1,2,6}, Keith D. Paulsen^{1,2,6}, and Kimberley S. Samkoe^{1,2,6*}

¹Thayer School of Engineering, Dartmouth College, Hanover, NH, United States

²Geisel School of Medicine, Dartmouth College, Hanover, NH, United States

³Department of Surgery, Dartmouth Hitchcock Medical Center, Lebanon, NH, United States

⁴Department of Pathology, Dartmouth Hitchcock Medical Center, Lebanon, NH, United States

⁵Department of Otolaryngology, Dartmouth Hitchcock Medical Center, Lebanon, NH, United States

⁶Translational Engineering in Cancer, Dartmouth Hitchcock Medical Center, Lebanon, NH, United States

* Correspondence:

Kimberley S. Samkoe

Kimberley.S.Samkoe@dartmouth.edu

Keywords: Radiomic analysis, Optomics, Fluorescence molecular imaging, Head and neck cancer, Epidermal growth factor receptor, Cancer detection.

Abstract

Background: Fluorescence molecular imaging is emerging as a method for precise surgical guidance during head and neck squamous cell carcinoma (HNSCC) resection. However, the tumor-to-normal tissue contrast is confounded by intrinsic physiological limitations of heterogeneous expression of the target molecule, epidermal growth factor receptor (EGFR), and the non-specific uptake of the fluorescent imaging agent.

Objective: In this study, we extended a radiomics approach for tissue classification to optical fluorescence molecular imaging data—termed “optomics”. Optomics seeks to improve tumor identification by leveraging textural pattern differences in EGFR expression conveyed by fluorescence. We determined whether these optomic signatures improve binary classification of malignant versus non-malignant tissues relative to more conventional fluorescence intensity thresholding.

Materials and Methods: Fluorescence image data collected through a Phase 0 clinical trial (NCT03282461) for testing ABY-029, a novel fluorescent EGFR-targeted imaging agent, involved 24 bread-loafed slices from surgical HNSCC resections originating from 12 patients who were stratified into three dose groups (30, 90, and 171 nanomoles). For analysis, each dose group was partitioned randomly 75%/25% into training/testing sets, then all training and testing sets were aggregated. A total of 1,472 standardized radiomic features were extracted from fluorescence image samples. A supervised machine learning pipeline involving a support vector machine classifier was trained with 25 top-ranked features selected by minimum redundancy maximum relevance criterion. Predictive performance of model was compared to fluorescence intensity thresholding by classifying testing set image patches of resected tissues with histologically confirmed malignancy status.

Results: The optomics approach provided consistent improvement in prediction accuracy on all testing set samples, irrespective of dose, compared to fluorescence intensity thresholding (mean accuracies of 89% vs. 81%; $P = 0.0072$).

Conclusions: The optomics approach outperformed conventional fluorescence intensity thresholding for tumor identification. Optomics mitigate diagnostic uncertainties introduced through physiological variability, imaging agent dose, and inter-patient biases of fluorescence molecular imaging by probing textural image information. The improved performance demonstrates that extending the radiomics approach to fluorescence molecular imaging data offers a promising image analysis technique for cancer detection in fluorescence-guided surgery.

1 Introduction

Head and neck squamous cell carcinomas (HNSCCs) account for approximately 900,000 cases worldwide and over 400,000 deaths annually (1). Surgical resection remains the first-line treatment for HNSCC. Cancer-free surgical margins with preservation of normal tissues are strongly associated with lower locoregional recurrence and improved patient outcomes (2). Unfortunately, achieving complete resection while minimizing unnecessary tissue removal is challenging due to tumor infiltration within sensitive head and neck anatomy. This clinical problem would benefit from precise intraoperative tumor identification and clear tumor-to-normal tissue differentiation during surgeries.

Over the past several years, near-infrared (NIR) fluorescence molecular imaging has entered the surgical theatre and shown promise for tumor identification during fluorescence-guided surgery (FGS) (3, 4). Optical tissue contrast is provided by differential uptake of the fluorescent agent in the tumor relative to surrounding normal tissues. Additionally, molecularly targeted fluorescent agents bind preferentially to receptors overexpressed in tumors, further increasing the fluorescence signal in cancers. Epidermal growth factor receptor (EGFR), a transmembrane cell surface glycoprotein associated with cell proliferation (5), is commonly expressed at high levels in a variety of epithelial tumors, including HNSCCs (>90%) (6-8), providing a strong rationale for investigating imaging agents that targets this receptor (9-11). Several have been studied in clinical trials and used in a variety of surgical applications (12-15).

In practice, fluorescence molecular imaging achieves modest optical tumor-to-normal ratios (16), which are not always representative of actual differences in cellular expression of EGFR among tumor and normal tissues (14, 17-19) due to confounding effects involved in the entire fluorescence process from illumination to detection. For example, noise and signal loss are introduced by imaging instruments, fluorophore photochemical events, and tissue-photon interactions (20). Several groups have developed methods to overcome these optical limitations through instrument and illumination optimization (21, 22). Physiologically, variability results from non-specific agent uptake in normal tissues (*i.e.*, non-specific binding in normal tissues with endogenously high EGFR expression like mucosa, salivary glands, and tonsils, and non-specific retention and perfusion of the agent caused by differences in vascular permeability) (23, 24) or from limited uptake in tumor tissues (*i.e.*, not all HNSCCs overexpress EGFR due to heterogeneous gene expression; or complex, macroscopic structures reduce agent diffusion in regions of necrosis) (25). To address these physiological effects, explorations of new probes (19, 26, 27), dosing strategies (18, 28-30), and innovative methods for quantitative molecular imaging (31-35) have increased tumor contrast. Computational image analyses also address imaging and physiological impacts on tumor contrast (36).

This study was motivated by observations of distinct fluorescence spatial patterns in EGFR expression in tumor versus normal tissues in HNSCC specimens shown in Figure 1. The effect was

corroborated by inspection of EGFR immunohistochemistry (IHC)-stained tissues that were spatially co-registered to fluorescence images (35). In general, the distribution of EGFR expression in normal tissues appeared homogeneous in intensity and spatially ordered, whereas it demonstrated heterogeneous staining intensity and spatial disorder in tumor. Leveraging these distinct spatial distributions of EGFR expression may yield contrast-enhanced visualization of tumor in HNSCCs relative to using fluorescence intensity alone, which by itself, does not incorporate spatial relationships or patterns in neighboring values.

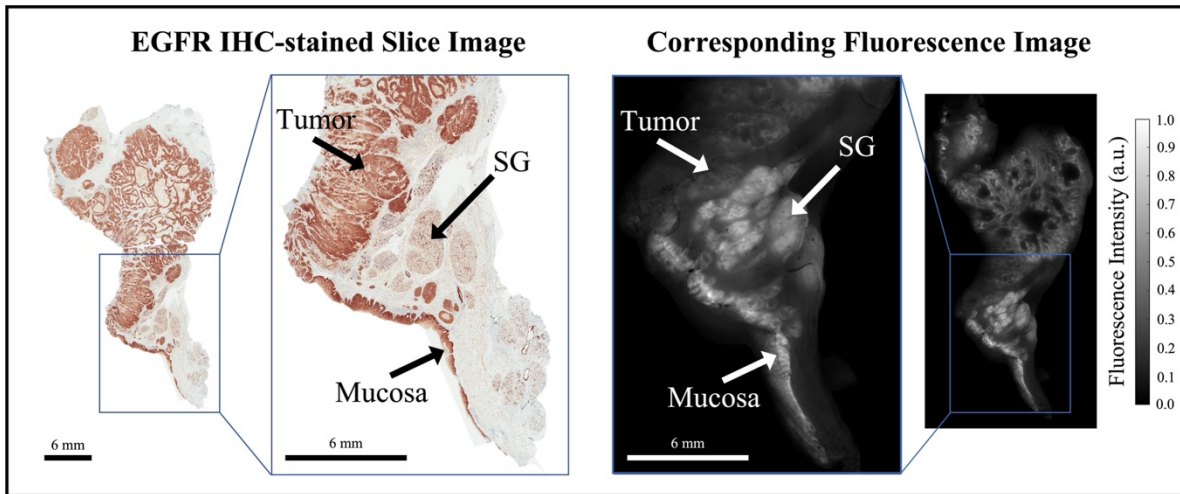


Figure 1. Representative bread-loafed slice of a head and neck cancer displaying normal and tumor-derived EGFR expression. EGFR IHC staining (*left*) and fluorescence (*right*) images of slice #16 from dose group 2. Arrows annotate EGFR-positive tissues including tumor, salivary gland (SG), and mucosa on the EGFR IHC staining and fluorescence images, respectively.

“Radiomics”, the high-throughput extraction and characterization of quantitative features from medical image data (37-39), generates first-order histogram statistics (*i.e.*, intensity metrics) in addition to second- and higher-order pixel statistics (*i.e.*, textures) (38). Radiomics also mines image features extracted for artificial intelligence (AI)-based decision support (40, 41), and has been used to detect disease and/or stratify tissues in conventional medical imaging data (*e.g.*, magnetic resonance imaging, computed tomography) (42-44). Streeter *et al.* applied the radiomics framework to multi-wavelength optical spatial frequency domain imaging (SFDI) of breast cancer tissues (45). Through extension of the “-omics” concept to high-dimensional optical imaging data, the authors proposed the term “optomics”, and developed a radiomics/optomics classification paradigm based on multimodal, micro-computed tomography and SFDI data that showed multimodal image feature sets improved detection of breast cancer samples compared to either modality alone. Similarly to radiomics, where application of large numbers of quantitative images features are mined to identify tumor phenotype as representations of its underlying genetic expression (42), applying optomics to EGRF-targeted fluorescence images may reveal spatial patterns in EGFR expression that are associated with native tissue/tumor genomic signatures.

In this study, an optomics analysis framework was developed to classify HNSCCs and normal tissues using EGFR-targeted fluorescence images of human surgical specimens derived for presurgical administration of the fluorescent molecule, ABY-029. The work evaluated the predictive performance of optomics analysis and compare it with conventional intensity-based thresholding for identifying HNSCC tissues in resected surgical specimens. Results suggest that encoding spatial relationships found in the fluorescence images by mining image data for quantitative high-

dimensional features identified tumor at surgical margins with superior diagnostic accuracy relative to intensity thresholding.

2 Materials and Methods

2.1 Clinical trial design

Data evaluated in this paper was acquired during a first-in-human, Phase 0, open-label, single-center, clinical trial of microdose evaluation of ABY-029 (exploratory Investigational New Drug (eIND) #122681) in head and neck cancer (ClinicalTrials.gov identifier: NCT03282461). The primary goal of the clinical study was to determine if microdose, or near microdose, administration ABY-029 lead to detectable fluorescence signals (defined as signal-to-background ratio, $SBR \geq 10$) in sampled EGFR-positive tissues. The peptide-fluorophore conjugate, ABY-029, consists of the EGFR-specific synthetic Affibody® peptide (Affibody AB, Solna, Sweden), conjugated to NIR fluorophore IRDye 800CW (LI-COR Biosciences, Inc., Lincoln, NE). The clinical protocol was approved by the Dartmouth-Hitchcock Health Institutional Review Board (D-HH IRB), and written informed consent was obtained from all patients. Further details of the trial eligibility criteria, and other protocol parameters for ABY-029 PHASE 0 trials can be found elsewhere (46).

Enrolled patients ($n = 12$) were assigned to one of three dose groups: Group 1 ($n = 3$) received 30 nanomoles/patient, Group 2 ($n = 3$) received 90 nanomoles/patient, and Group 3 ($n = 6$) received 171 nanomoles/patient. Dose escalation occurred if the first three patients of the 30 and 90 nanomole test groups did not achieve $SBR \geq 10$. Table 1 summarizes the clinical trial dose groups and patient characteristics.

Table 1. Dose groups and patient characteristics.

| | Patient index | Age | Gender | Cancer site | Number of bread-loafed slices |
|---|---------------|-----|--------|------------------------------|-------------------------------|
| Group 1 (30 nanomoles/patient) | 1 | 45 | M | Right tonsil, base of tongue | 6 |
| | 2 | 59 | M | Oropharynx – soft palate | 2 |
| | 3* | 60 | M | Tongue | 0 |
| Group 2 (90 nanomoles/patient) | 4 | 55 | F | Buccal mucosa | 3 |
| | 5 | 56 | F | Tongue | 4 |
| | 6 | 50 | F | Retromolar trigone | 1 |
| Group 3 (171 nanomoles/patient) | 7 | 60 | M | Floor of mouth | 1 |
| | 8 | 59 | M | Tongue | 1 |
| | 9 | 82 | F | Buccal mucosa | 2 |
| | 10 | 45 | F | Retromolar trigone | 1 |
| | 11 | 48 | M | Oropharynx | 1 |
| | 12 | 86 | M | Tongue | 2 |

* Surgical specimens collected from the third patient did not have corresponding pathology images for later analysis.

2.2 Post-resection surgical specimen processing

The gross primary tumor specimens were sectioned into bread-loafed slices (5 mm slice thickness), according to standard-of-care. Each bread-loafed slice was imaged using the 800-nm channel of the Odyssey CLx (LI-COR Biosciences, Inc., Lincoln, NE) at 42- μ m pixel resolution. Formalin-fixed paraffin-embedded (FFPE) blocks were created and sectioned (4 μ m thickness). Hematoxylin and eosin (H&E) and EGFR IHC slides were obtained from consecutive 4- μ m sections taken from the imaged tissue surface. The histology slides were examined by a board-certified pathologist (L.J.T.), who delineated tumor regions of interest (ROIs) on each slide. Slides were imaged with and without the tumor ROIs at 20x magnification using an Aperio AT2 DX System (Leica Biosystems, Wetzlar, Germany). Tumor ROIs were co-registered with the fluorescence images by overlaying the greyscale fluorescence and H&E images and digitally annotating the former with respect to the latter using a custom MATLAB script (vR2021b, MathWorks, Natick, MA). Figure 2 illustrates the clinical workflow for an enrolled study subject and includes representative images of surgical specimens at each stage of the process.

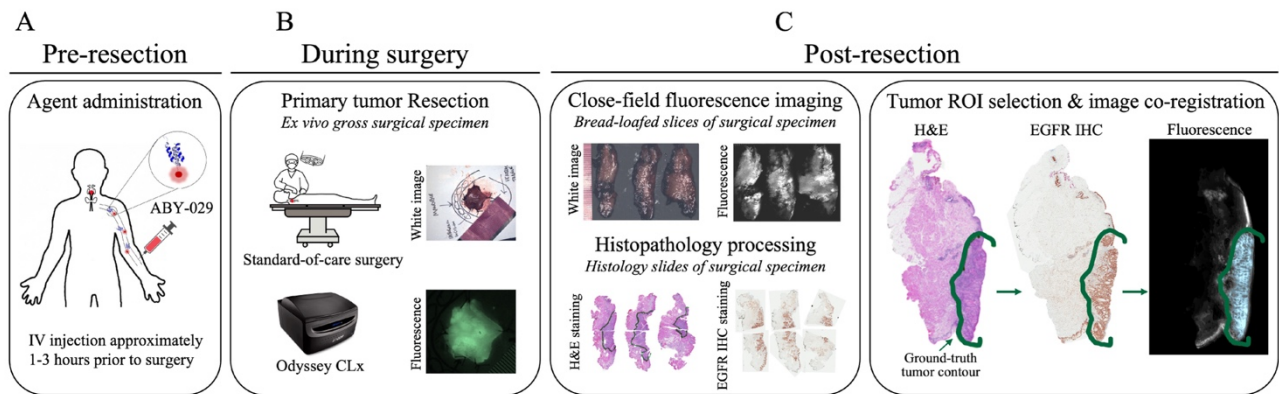


Figure 2. Clinical trial workflow. (A) ABY-029 was administered via 5 ml intravenous bolus injection 1-3 hours prior to surgery. (B) Each patient underwent stand-of-care surgery, and gross surgical specimens were collected. (C) After surgery, specimens were sectioned in bread-loafed slices, FFPE, then cut into consecutive slides for staining. Close-field fluorescence imaging was performed on the bread-loafed slices. Histology slides from bread-loafed slices underwent standard histopathological examination, providing tissue ROI ground truth.

2.3 Design of image classification techniques

2.3.1 Image pre-processing

Each fluorescence image was background subtracted and normalized to a fluorescence calibration target placed in the field-of-view of every image. The process eliminated day-to-day instrument-specific variations (47, 48), which would confound comparisons of fluorescence data obtained during the trial. The background-subtracted and calibrated image was normalized by rescaling the intensity range to [0,1], which eliminated the inter-slice fluorescence bias caused by variations in imaging agent dose and heterogeneous patient characteristics. The image normalization step was also necessary for optic feature extraction which requires a consistent range of intensities across image samples. Figure 3 shows representative examples of the histological and fluorescence image data analyzed, including three bread-loafed slices from the three dose groups. The fluorescence intensity levels of the standardized fluorescence images in the bottom row exhibit relatively uniform values for the three dose groups.

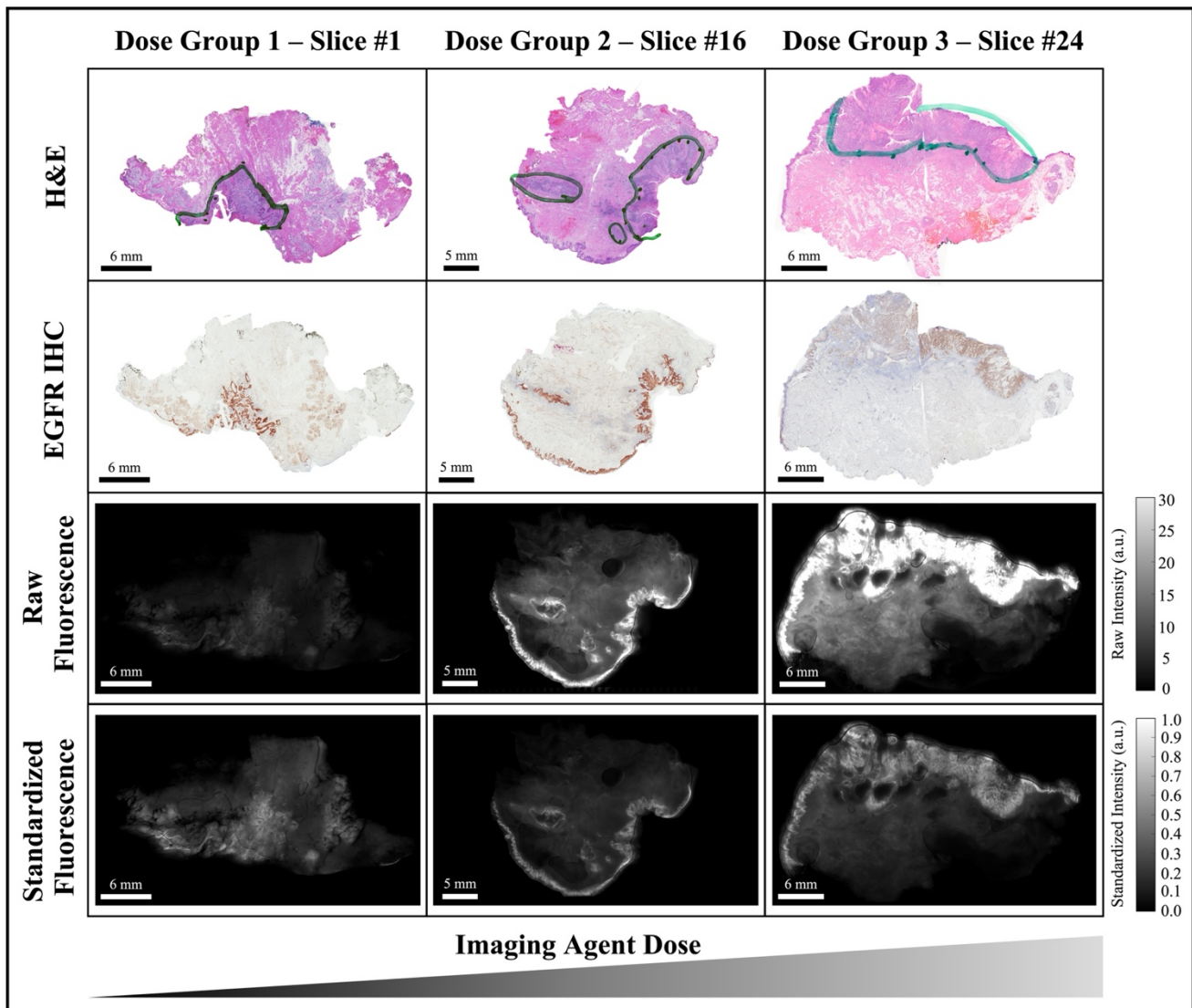
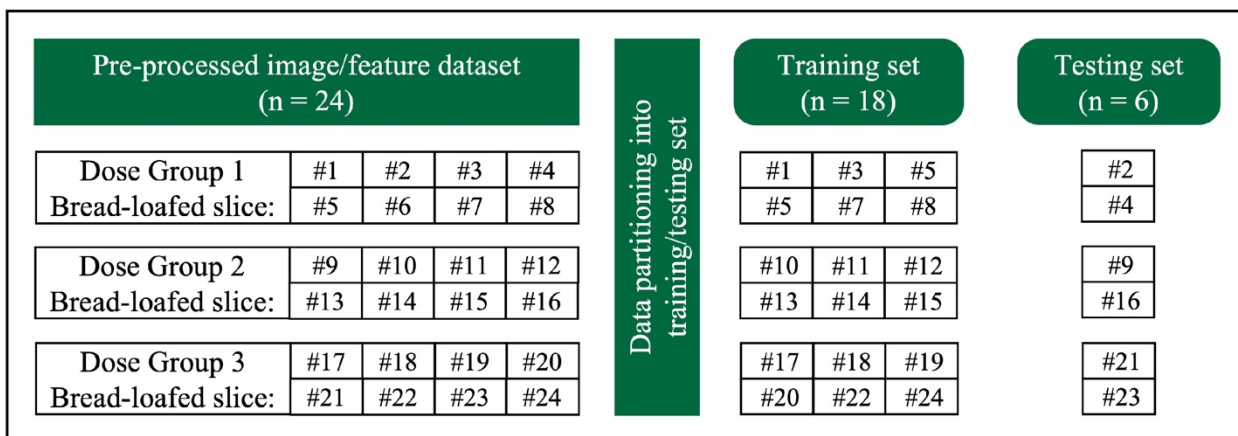


Figure 3. Representative bread-loaf slices from the three dose groups (30, 90, and 171 nanomoles). Green contours in the H&E images indicate ground-truth tumor regions delineated by the pathologist (author L.J.T.). The bottom two rows show comparisons of fluorescence images before (raw fluorescence) and after image pre-processing (standardized fluorescence).

2.3.2 Data partitioning strategy

Data were partitioned into training and testing sets at the level of 24 fluorescence bread-loafed-slice images (8 slices in each dose group). Slices were distributed randomly into training/testing sets with a 75%/25% distribution (6 and 2 slices in training and testing sets, respectively) for each dose group (18 and 6 slices in aggregate) and analyzed with the fluorescence thresholding and optomics methods described in the following sections. Figure 4 summarizes the data partitioning and indexing of bread-loafed slices in the training/testing sets along with the two image processing workflows (thresholding and optomics).

A



B

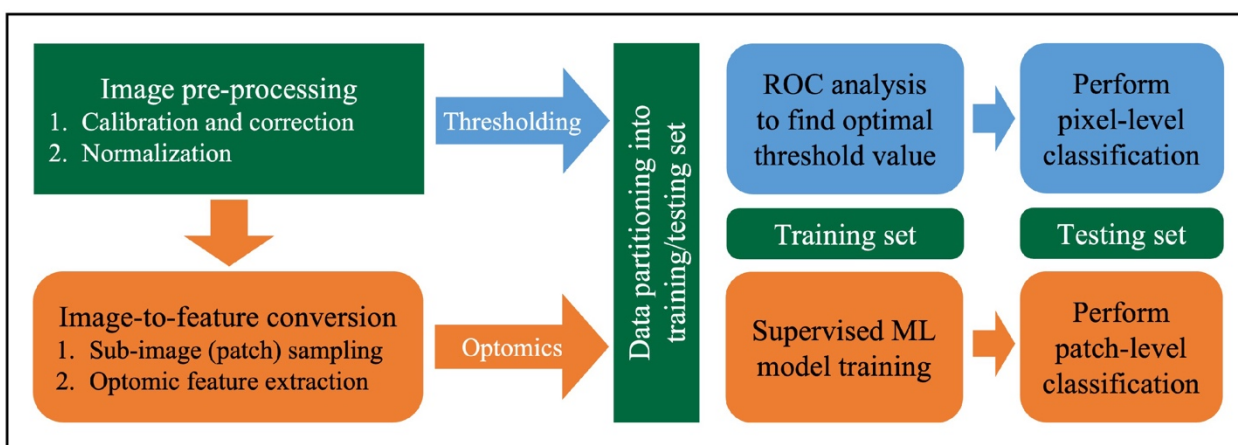


Figure 4. Image analysis workflow. (A) Data partitioning strategy. Bread-loafed slices were partitioned 75%/25% into aggregated training and testing data. The same slice-level partitioning strategy was used to assess the performance of both methods. (B) Workflow comparison of thresholding and optomics methods. Green modules indicate steps shared by the two methods. Blue and orange modules represent the steps to distinct to the thresholding and optomics approaches, respectively.

2.3.3 Fluorescence intensity thresholding method

Fluorescence intensity thresholding uses image intensity values as the discriminator and is a typical way to perform binary classification of tissue types using fluorescence imagery (49-51). Receiver operator characteristic (ROC) curves were created from the fluorescence image data using the pathologist-defined ROIs as ground truth and by varying the intensity threshold. An optimum cutoff point (OCP) was selected based on the maximum pixel-level classification accuracy achieved on the training set. Figure 4B describes intensity-based thresholding scheme (blue boxes) performed in this study.

2.3.4 Optomics method

Optomic features were computed on the sub-image (or patch) level. Sub-image sampling was implemented prior to feature extraction to enlarge the dataset for model training and enabled patch-level classification and performance comparisons with pixel intensity thresholding. The sub-image

sampling randomly picked a center pixel in each tissue ROI and expanded the center pixel location into a square patch. After sub-image sampling, optomic features were extracted using the *PyRadiomics* package (v3.0.1) (52), which is open-source and Image Biomarker Standardization Initiative (IBSI)-compliant (53). A total of 1,472 *PyRadiomics* features were extracted from each sampled patch. Features included first-, second-, and higher-order pixel statistics (40). Eighteen (18) first-order features (*i.e.*, histogram statistics) described the distribution of intensities of individual pixels. A total of 74 second- and higher-order features were quantified, which captured the statistical interrelationships between sets of two or more pixels. In addition to extracting these 92 features from the original patch, fifteen image filters were applied and the same 92 features were extracted from each filtered patch. Further details on these *PyRadiomics* features are described in the supplementary material. In summary, each wide-field fluorescence image of a bread-loafed tissue slice was represented by a group of sub-images, and each sub-image was characterized by a total of 1,472 optomic features (92 original image patch features + 15 filters \times 92 features/filter). Figure 4B illustrates the steps involved in the optomics method (orange boxes).

A conventional machine learning (ML) classifier was trained using image patches with ground truth tumor and normal tissue labeling, and its classification performance was evaluated on the testing set. To reduce over-fitting in high-dimensional feature space derived from a limited number of samples, a feature selection step was included in which top-ranked optomic features were selected in a grid search for model fitting (instead of using the entire 1,472 optomic feature set). Coding details are discussed in the supplementary material. Three hyperparameters in the ML pipeline were tuned: ML classifier type, feature selection algorithm, and number of top-ranked optomic features. Leave-One-Out Cross-Validation (LOOCV) was performed on the training set (*i.e.*, 18-fold CV) for hyperparameter tuning. LOOCV holds a group of patch feature data from a single slice as the validation set for each split. LOOCV mean accuracy of each hyperparameter combination was obtained by averaging the validation specimen accuracies across all splits. The hyperparameter combination that generated the highest LOOCV mean accuracy was chosen as the final ML pipeline for model training and testing. The process of determining the best performing hyperparameter combination is summarized in Supplementary Figure 1.

2.4 Statistical analysis

Statistical analysis was performed using a two-sided paired t-test for the prediction accuracy difference between the two image classification methods (*i.e.*, thresholding versus optomics) on the six wide-field fluorescence images of bread-loafed slices from the testing set. All statistical testing was implemented in MATLAB (vR2021b, MathWorks, Natick, MA). A *P* value of 0.05 or less was considered statistically significant.

3 Results

3.1 ML pipeline hyperparameter optimization and optomic feature selection

Three hyperparameters were explored: (1) ML classifier type, (2) feature selection algorithm, and (3) number of top-ranked features selected. Seven ML classifier types and seven feature selection algorithms were evaluated based on their popularity, simplicity, and computational efficiency, as reported in the literature (54, 55). ML classifier types included random forest (RF), *k*-nearest neighbors (*k*NN), decision tree (DT), support vector machine (SVM), boosting (BST), Bayesian (BY), and discriminant analysis (DA). Feature selection algorithms were minimum redundancy maximum relevance (MRMR), Fisher score ranking (FSCR), Chi-square ranking (CHSQ), Gini index ranking (GINI), mutual information maximization (MIM), Spearman ranking correlation coefficient

(SRCC), and Pearson ranking correlation coefficient (PRCC). The number of top-ranked features selected was investigated by choosing 5 to 100 features in increments of 5 (*i.e.*, $\{5k \mid k \in \mathbb{Z}, 1 \leq k \leq 20\}$).

Each combination of hyperparameters was evaluated through LOOCV of the training set (*i.e.*, 7 classifiers \times 7 feature selection methods \times 20 options of feature numbers = 980 combinations). LOOCV involved 18 folds (because the training set had 18 individual slices). Mean validation accuracy from the 18-fold LOOCV was chosen to describe the performance of each hyperparameter combination. After iterating through all hyperparameter combinations, the one with the highest LOOCV mean accuracy was considered to be optimal and became the final ML pipeline. Figure 5A depicts the LOOCV mean accuracies achieved by every combination of ML classifier type (rows) and feature selection algorithm (columns) when 25 top-ranked features were used. Heatmaps for different numbers of selected features were similarly produced in this two-dimensional format, leading to a three-dimensional LOOCV mean accuracy representation over all combinations of the three hyperparameters. LOOCV mean accuracy heatmaps corresponding to other numbers of selected features are reported in Supplementary Figures 2A-2S. The combination of SVM classifier and MRMR feature selection algorithm yielded the overall highest accuracies, as shown in Supplementary Figure 2T. LOOCV mean accuracy increased with increasing number of features, as displayed in Supplementary Figure 2U. To limit overfitting effects and minimize computational time, the optimal number of selected features was taken as the fewest selected features in the validation accuracy tolerance region (mean \pm 1.5 standard deviation of plateau values). Thus, the final hyperparameter combination was a SVM classifier, MRMR feature selection algorithm, and 25 top-ranked features which provided a LOOCV mean accuracy of $84\% \pm 13\%$.

Figure 5B visualizes the entire high-dimensional optomics feature set extracted from training set data in a hierarchically clustered heatmap. Optomic features corresponding to training set sub-image samples were standardized to Z-scores. Two dominant clusters of sub-image samples exist, one containing mainly normal samples and one containing mainly tumor samples (84% normal in Cluster 1; 82% tumor in Cluster 2) which indicate that optomic features extracted from fluorescence images have potential to classify tissue malignancy with high fidelity.

Figure 5C shows the distribution of tabulated optomic features selected by MRMR in each of 18 LOOCV folds. The most frequently selected features were all filter-based features, and all but four were second- or higher-order statistics, indicating that textural information was overwhelmingly favored by MRMR feature selection for separating malignant from non-malignant samples.

Sub-image patch size is an important pipeline hyperparameter that was investigated independently, and prior to the hyperparameter tuning described above, by considering three possibilities: 0.88 mm \times 0.88 mm, 1.39 mm \times 1.39 mm, and 1.81 mm \times 1.81 mm. Results presented in this paper were derived from 1.81 mm \times 1.81 mm sub-image patches unless otherwise specified because it leads to the best classification performance (Supplementary Figure 3). Combining training results from the three sub-image patch sizes is discussed in Section 3.3.

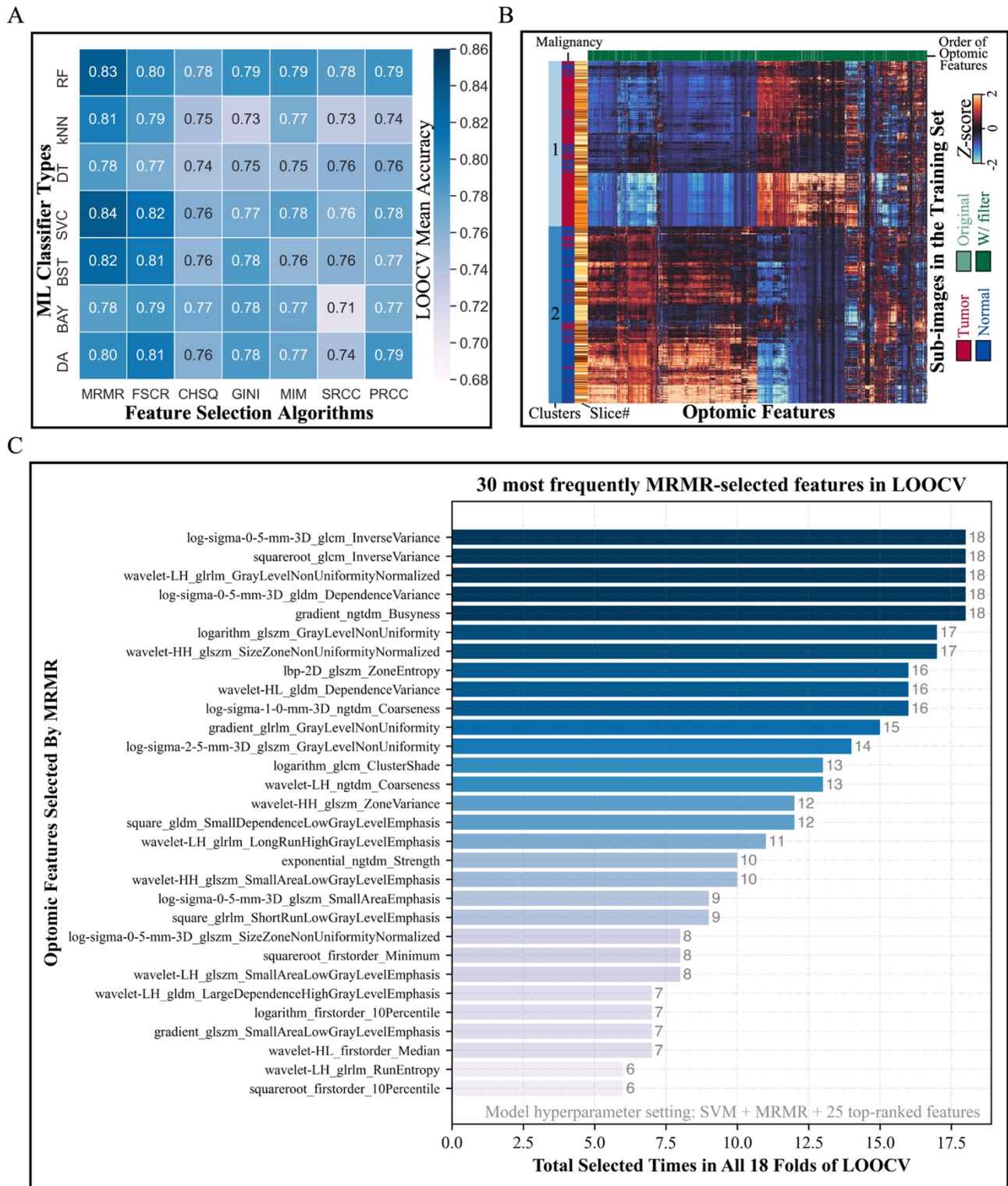


Figure 5. Model hyperparameter optimization through LOOCV and feature selection. (A) Heatmap depicts the LOOCV mean accuracy achieved by different combinations of classifiers (rows) and feature selection algorithms (columns) when 25 top-ranked features were used. The combination of SVM classifier and MRMR feature selection showed the highest validation accuracy. (B) Hierarchical clustering of training set sub-image patches (5,470 total; vertical axis) and optic features (1,472 total; horizontal axis) reveals natural groupings of tissue types. (C) Most frequently

selected features by MRMR with the optimal hyperparameters combination during LOOCV. Horizontal axis represents the number of times that each optomic feature was selected by MRMR in all 18 folds of LOOCV. All tabulated features were filter-based, and all but four were second- and higher-order statistics.

3.2 Comparison of thresholding and optomics classification methods

Evaluation of binary classification performance of thresholding applied the OCP value, determined on the training set through ROC analysis (OCP = 0.155, Figure 6A), to every pixel in the bread-loafed-slice fluorescence images in the test set. By comparing threshold prediction results pixel-by-pixel to ground truth confirmed from co-registered H&E image data, accuracy was determined to be 79.7%. Of note, the false negative rate (FNR) of 25.0% indicates that the method suffers from relatively low sensitivity. Figure 6A shows typical thresholding results on a specimen in the test set.

Optomics classification performance on the same test set specimen appears in Figure 6B. Importantly, optomics classification was performed on the patch-level (not on the pixel-level like thresholding) because the texture-based optomic features were extracted on patches that contained multiple pixels. Optomics achieved an accuracy of 93.5% and an FNR that was an order of magnitude lower than that of the thresholding method (2.5%) on the same test set specimen. The comparison of classification performances of two methods for the other five test set specimens is displayed in Supplementary Figure 4.

Figure 7 compares prediction performances of thresholding and optomics classification methods on all six test set specimens in which a statistically significant difference in prediction accuracy was found based on a two-tailed, paired t-test ($P = 0.0072$). Optomics improved prediction performance in every test set slice relative to thresholding (mean improvement was 7.5%). Additionally, the interquartile range of thresholding prediction accuracies was larger than the optomics method.

3.3 Optomics method prediction probability map

To visualize optomics method prediction results on a pixel-level, a pseudocolor-coded heatmap (49) of model prediction probability was created and overlaid on the original greyscale fluorescence image. The continuous, pixel-level visualization was generated through biharmonic spline interpolation of the patch-level model probabilities assigned to the patch center pixel (using *v4; griddata*, implemented in MATLAB, vR2021b, MathWorks, Natick, MA). Figure 8A demonstrates the process of assigning the patch-level predicted probabilities to patch center pixels, and Figure 8B shows a pseudocolor visualization of the probability map overlaid on the greyscale fluorescence image.

To reduce bias introduced by assigning the patch-level predicted probability to the center pixel, independent ML models (with optimized hyperparameters) were generated from square patches with three different sizes (1.81, 1.39, and 0.88 mm side length) surrounding the same center pixel (Figure 8C, see Supplementary Figure 5 for ML model process for different patch sizes). The final center pixel probability was determined by averaging the predicted probabilities from the ML models with the three patch sizes. Figure 8D shows the interpolated probability map from the prediction outputs from the three patch sizes in comparison to Figure 8B generated from a single patch size (1.81 mm²). The number of pixels with high tumor probability (visualized in yellow) but outside the ground truth tumor ROI decreased, while the number of those inside the ground truth-tumor ROI increased when multiple patch sizes were included in the analysis. Optomics method prediction probability maps of the other five testing slices are shown in Supplementary Figure 6.

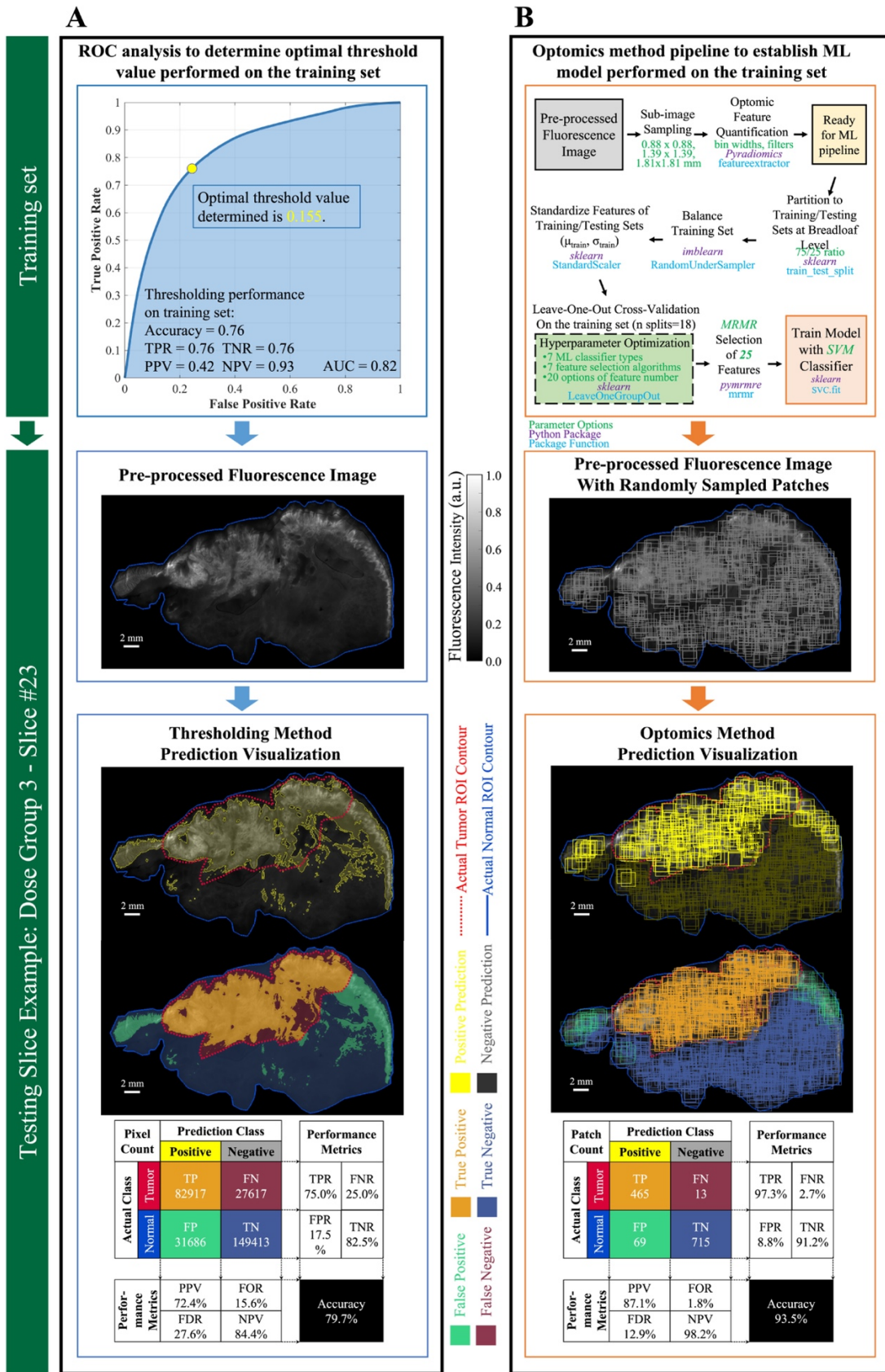


Figure 6. Performance evaluation of thresholding versus optomics methods. (A) Thresholding method and its classification performance. Optimum cutoff point (*i.e.*, threshold value) was

determined through ROC analysis on the training set and its predictive performance was assessed on the testing set. Pixel-level classification of the thresholding method is visualized on a testing slice example. Metrics describing its predictive performance on this testing slice example are summarized in the confusion matrix. (B) Optomics method and its classification performance. The ML model was determined based on the training set and a supervised ML pipeline summarized in the flow chart. Patch-level classification of the optomics method is visualized on the same testing slice and its predictive performance is summarized in the confusion matrix.

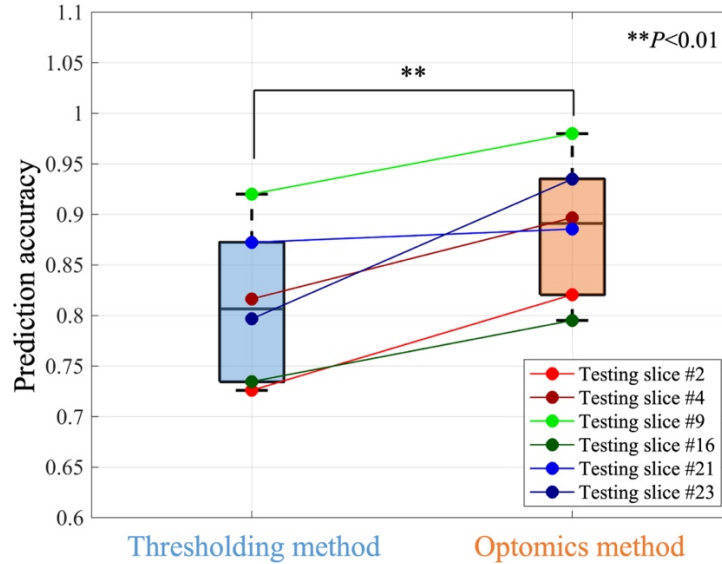


Figure 7. Comparison of the prediction performance of thresholding and optomics methods based on all testing slices.

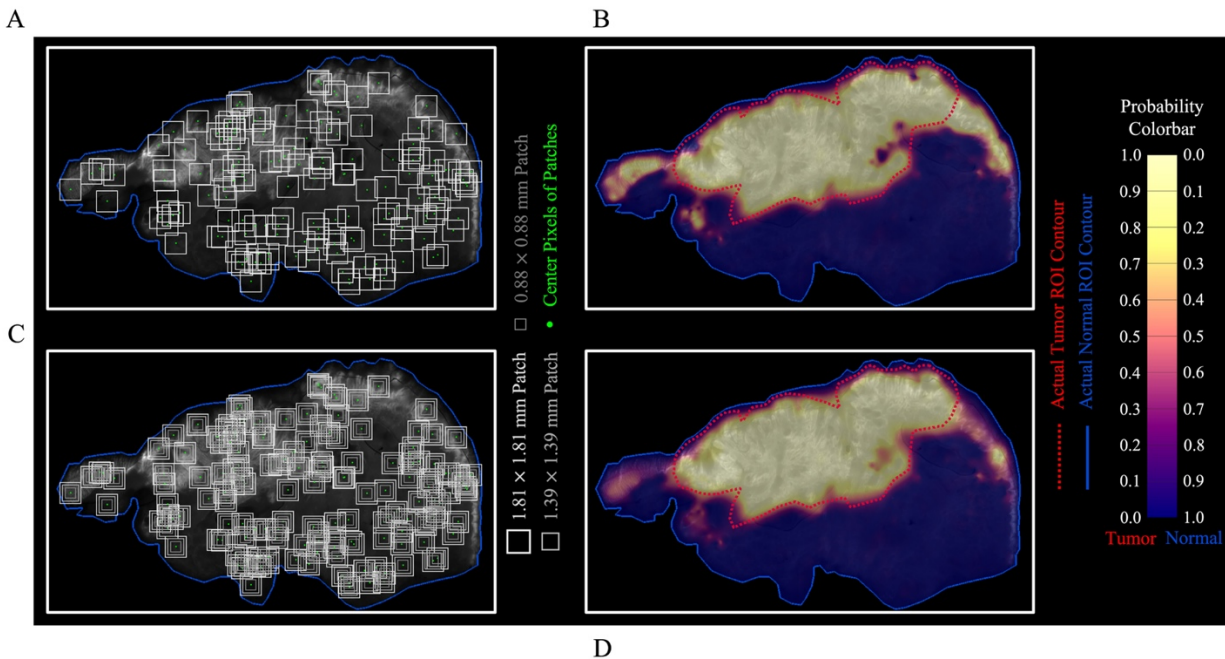


Figure 8. Optomics method predicted continuous probability maps. (A-B) Single patch size sampling and its probability map. (C-D) Three patch size sampling and the combined probability map based on the average probability derived from the three patch sizes.

4 Discussion

Tissue heterogeneity is a hallmark of cancer that is detrimental to successful patient outcomes (56). Radiomics have proved promising for mining spatial information across tumor volumes to generate diagnoses and inform decision making (40, 57-59) in the face of tumor heterogeneity, and radiomic features have been correlated with tissue heterogeneity, tumor aggressiveness, and even treatment response (60-63). Recently, Streeter *et al.* demonstrated application of radiomic analysis to optical imaging data, termed “optomics,” for breast tumor detection (45). The authors found that combining radiomic and optomic feature sets, which were extracted from two imaging modalities (*i.e.*, micro-CT and optical SFDI), improved breast cancer detection accuracy over either modality alone. Here, the optomics paradigm was applied to spatial patterning of EGFR based on fluorescence imaging of HNSCCs through a targeted molecular marker, ABY-029.

In this study, prediction outcomes from optomics were compared directly to those obtained from fluorescence intensity thresholding for tumor delineation. Optomics leverage high-throughput feature extraction to derive textural image information which reflects pixel relationships to structural tissue characteristics that have been shown to provide high prognostic power in other radiomic settings (64-67). Thresholding is employed commonly in fluorescence-guided surgery (16, 50, 51, 68, 69), but the approach is insensitive to spatial patterns of fluorescence that may be related to tissue types or disease states. In fact, heterogeneous fluorescence intensity in regions of interest limit image contrast because of high signal variability (70). Additionally, physiological factors and non-specific binding confound direct relationships between fluorescence signals and tumor location.

The fundamental difference between thresholding and optomics methods lies in the extraction of image features for tissue classification. While thresholding uses pixel intensities for tumor differentiation, optomics exploit inter-pixel spatial relationships and higher dimensional image textures to achieve the same end. Optomics resulted in a mean improvement of 7.5% in prediction accuracy relative to intensity thresholding based on the same training and testing data ($P = 0.0072$). This improvement in prediction performance is proof of principle for how spatial and textural image features enhance tissue type identification from fluorescence molecular imaging.

Threshold prediction accuracies demonstrated high variation when based on a single threshold value determined from training images and may be due to inter-patient or inter-specimen bias or differences in fluorescence signals between dose groups. Data from three dose groups were involved in the study (30, 90, and 171 nanomoles per patient), but differences in subject body-mass-index were not evaluated. Fluorescence image normalization reduced variations in inter-patient signals and amplified differences in normal and tumor fluorescence, but inhomogeneous overexpression of EGFR in tumor and high endogenous expression of EGFR in normal tissues still have confounding effects on fluorescence signals, which is evident in the overlapping regions of intensity histograms from ground truth tumor and normal tissue ROIs displayed in Supplementary Figure 7. Inability to separate fluorescence signals between normal tissues and tumor caused the low classification accuracy of the thresholding method. Optomics were less affected by variations in imaging agent dose and inter-image bias based on the higher FPR and FNR achieved (Supplementary Figure 4B). False positive predictions were mainly located in normal tissues that had high endogenous EGFR expression. This result is observed in Figure 6, where visualized predictions demonstrate that optomics successfully identified normal EGFR expressing mucosa, found along the edges of the specimens, while the fluorescence thresholding method failed to identify these regions accurately. False negative predictions were found in tumor tissues with low or heterogeneous expression of EGFR (*i.e.*, tumor necrosis in the interior of ROIs). Optomics identified these low fluorescing tumor

tissues more effectively, which decreased the overall FN predictions compared to fluorescence thresholding. Decreases in FPR and FNR demonstrate the potential value of incorporating spatial information when detecting tumor tissues.

Visualization of tumor extent and its boundary with normal tissues is critical in FGS and has been investigated extensively (16, 50, 51, 68, 69, 71). Here, a continuous tumor probability map was generated at the pixel level by interpolating predicted probabilities from center pixels of sampled patches. Production of probability maps from optomics analysis may provide a decision guide for surgeons. The probability output may be able to map the surface of the entire surgical specimen surface to identify areas suspicious for residual disease. Ideally, surgeons would threshold probability maps based on confidence intervals, their experience, and the desired goals for surgery. Probability outputs from ML models may be able to assist surgeons in achieving complete resections more often, and thereby achieve improved patient outcomes.

The small size of the image dataset which was used to train and evaluate the predictive performance of the ML-based optomics method limited its power to distinguish tissue types and the generalizability of the trained model as a classification tool. The number of fluorescence images of bread-loafed slices ($n = 24$) and number of patients ($n = 12$) was modest. The test set only included six specimens, two of which were from a single patient. In the future, more data would allow patient level instead of slice level partitioning. Comparisons between thresholding and optomics methods also introduced bias because of disparities in the data sampling; the former performed pixel-level classification while the latter produced patch-level classification. The difference may influence the validity of comparing their prediction performance. Generation of an interpolated pixel-level probability map by averaging across optomics results from difference patch sizes may mitigate the influence of these differences. Deformation of tissue between fresh bread-loafed specimens for NIR fluorescence imaging and formalin-fixed, paraffin embedded sections for histologic examination makes precise co-registration of these images difficult, if not impossible, to achieve, and thus, limited the accuracy of ROIs transferred from H&E to fluorescence images. Leveraging inter-patch spatial relationships by assuming adjacent sub-images have higher probability of containing similar texture patterns and sharing the important correlative information, may enhance the optomics method performance even further.

This study advances an optomics analysis paradigm for classifying fluorescence image data in HNSCC specimens. Relative to conventional fluorescence intensity thresholding, optomics increased the accuracy of tumor identification and provided more precise tumor mapping for surgical guidance. Optomic signatures have potential to reveal underlying image features that are not apparent to the human observer. The performance of optomic in HNSCC detection reported here suggests that extending the approach to fluorescence molecular imaging data offers a promising image analysis technique for cancer detection during FGS in other settings.

5 Conflict of Interest

ABY-029 was developed through an academic-industrial partnership, funded through CA167413 with Affibody AB and LI-COR Biosciences, Inc. The authors have no other conflict to report.

6 Author Contributions

K.S.S., K.D.P., B.W.P., Y.C. and S.S.S. conceptualized the study. Y.C., S.S.S., B.H. and K.S.S. designed the study. K.S.S., H.S.S., J.R.G. and L.J.T. performed the experiments. J.A.P. performed the surgery. Y.C., S.S.S., K.S.S., B.H. and H.S.S. analyzed the data. B.W.P., K.D.P. and K.S.S.

provided supervision. S.S.S., B.W.P., K.D.P. and K.S.S. provided the funding. Y.C. drafted the manuscript, and all authors reviewed the manuscript.

7 Funding

This study was funded by the National Cancer Institute (NCI) R37 Early Investigator MERIT Award (CA212187) and F31 fellowship grant (CA257340). ABY-029 manufacturing was funded by NCI R01 CA167413.

8 Acknowledgments

We would like to acknowledge Sally B. Mansur for clinical and research support.

9 Supplementary Material

The supplementary material is available to download at <https://dropbox.thayer.dartmouth.edu/2e810bf2fbd6be3b7ee587af71b00a4e>.

10 Data Availability Statement

The datasets presented in this article are not readily available because of participant privacy concerns. Requests to access the datasets should be directed to Kimberley.S.Samkoe@dartmouth.edu.

11 References

1. Siegel RL, Miller KD, Fuchs HE, Jemal A. Cancer statistics, 2022. *CA Cancer J Clin.* 2022;72(1):7-33.
2. McMahan J, O'Brien CJ, Pathak I, Hamill R, McNeil E, Hammersley N, et al. Influence of condition of surgical margins on local recurrence and disease-specific survival in oral and oropharyngeal cancer. *Br J Oral Maxillofac Surg.* 2003;41(4):224-31.
3. Vahrmeijer AL, Hutteman M, van der Vorst JR, van de Velde CJ, Frangioni JV. Image-guided cancer surgery using near-infrared fluorescence. *Nat Rev Clin Oncol.* 2013;10(9):507-18.
4. Nagaya T, Nakamura YA, Choyke PL, Kobayashi H. Fluorescence-Guided Surgery. *Front Oncol.* 2017;7:314.
5. Wieduwilt MJ, Moasser MM. The epidermal growth factor receptor family: biology driving targeted therapeutics. *Cell Mol Life Sci.* 2008;65(10):1566-84.
6. Sigismund S, Avanzato D, Lanzetti L. Emerging functions of the EGFR in cancer. *Mol Oncol.* 2018;12(1):3-20.
7. Zhou Q, van den Berg NS, Rosenthal EL, Iv M, Zhang M, Vega Leonel JCM, et al. EGFR-targeted intraoperative fluorescence imaging detects high-grade glioma with panitumumab-IRDye800 in a phase 1 clinical trial. *Theranostics.* 2021;11(15):7130-43.
8. Zimmermann M, Zouhair A, Azria D, Ozsahin M. The epidermal growth factor receptor (EGFR) in head and neck cancer: its role and treatment implications. *Radiat Oncol.* 2006;1:11.
9. Salomon DS, Brandt R, Ciardiello F, Normanno N. Epidermal growth factor-related peptides and their receptors in human malignancies. *Crit Rev Oncol Hematol.* 1995;19(3):183-232.

10. Hoopes PJ, Petryk AA, Tate JA, Savellano MS, Strawbridge RR, Giustini AJ, et al. Imaging and modification of the tumor vascular barrier for improvement in magnetic nanoparticle uptake and hyperthermia treatment efficacy. *Proc SPIE Int Soc Opt Eng.* 2013;8584.
11. Grandis JR, Tweardy DJ. Elevated levels of transforming growth factor alpha and epidermal growth factor receptor messenger RNA are early markers of carcinogenesis in head and neck cancer. *Cancer Res.* 1993;53(15):3579-84.
12. Nguyen QT, Tsien RY. Fluorescence-guided surgery with live molecular navigation--a new cutting edge. *Nat Rev Cancer.* 2013;13(9):653-62.
13. Heath CH, Deep NL, Sweeny L, Zinn KR, Rosenthal EL. Use of panitumumab-IRDye800 to image microscopic head and neck cancer in an orthotopic surgical model. *Ann Surg Oncol.* 2012;19(12):3879-87.
14. Rosenthal EL, Warram JM, de Boer E, Chung TK, Korb ML, Brandwein-Gensler M, et al. Safety and Tumor Specificity of Cetuximab-IRDye800 for Surgical Navigation in Head and Neck Cancer. *Clin Cancer Res.* 2015;21(16):3658-66.
15. Warram JM, de Boer E, Sorace AG, Chung TK, Kim H, Pleijhuis RG, et al. Antibody-based imaging strategies for cancer. *Cancer Metastasis Rev.* 2014;33(2-3):809-22.
16. Gao RW, Teraphongphom NT, van den Berg NS, Martin BA, Oberhelman NJ, Divi V, et al. Determination of Tumor Margins with Surgical Specimen Mapping Using Near-Infrared Fluorescence. *Cancer Res.* 2018;78(17):5144-54.
17. Gao RW, Teraphongphom N, de Boer E, van den Berg NS, Divi V, Kaplan MJ, et al. Safety of panitumumab-IRDye800CW and cetuximab-IRDye800CW for fluorescence-guided surgical navigation in head and neck cancers. *Theranostics.* 2018;8(9):2488-95.
18. Nishio N, van den Berg NS, van Keulen S, Martin BA, Fakurnejad S, Zhou Q, et al. Optimal Dosing Strategy for Fluorescence-Guided Surgery with Panitumumab-IRDye800CW in Head and Neck Cancer. *Mol Imaging Biol.* 2020;22(1):156-64.
19. Voskuil FJ, de Jongh SJ, Hooghiemstra WTR, Linssen MD, Steinkamp PJ, de Visscher SAHJ, et al. Fluorescence-guided imaging for resection margin evaluation in head and neck cancer patients using cetuximab-800CW: A quantitative dose-escalation study. *Theranostics.* 2020;10(9):3994-4005.
20. Leblond F, Davis SC, Valdés PA, Pogue BW. Pre-clinical whole-body fluorescence imaging: Review of instruments, methods and applications. *J Photochem Photobiol B.* 2010;98(1):77-94.
21. Hu Z, Fang C, Li B, Zhang Z, Cao C, Cai M, et al. First-in-human liver-tumour surgery guided by multispectral fluorescence imaging in the visible and near-infrared-I/II windows. *Nat Biomed Eng.* 2020;4(3):259-71.
22. Troyan SL, Kianzad V, Gibbs-Strauss SL, Gioux S, Matsui A, Oketokoun R, et al. The FLARE intraoperative near-infrared fluorescence imaging system: a first-in-human clinical trial in breast cancer sentinel lymph node mapping. *Ann Surg Oncol.* 2009;16(10):2943-52.
23. Carmeliet P, Jain RK. Angiogenesis in cancer and other diseases. *Nature.* 2000;407(6801):249-57.
24. Maeda H, Wu J, Sawa T, Matsumura Y, Hori K. Tumor vascular permeability and the EPR effect in macromolecular therapeutics: a review. *J Control Release.* 2000;65(1-2):271-84.

25. Lammerts van Bueren JJ, Bleeker WK, Bøgh HO, Houtkamp M, Schuurman J, van de Winkel JG, et al. Effect of target dynamics on pharmacokinetics of a novel therapeutic antibody against the epidermal growth factor receptor: implications for the mechanisms of action. *Cancer Res.* 2006;66(15):7630-8.
26. Elliott JT, Dsouza AV, Marra K, Pogue BW, Roberts DW, Paulsen KD. Microdose fluorescence imaging of ABY-029 on an operating microscope adapted by custom illumination and imaging modules. *Biomed Opt Express.* 2016;7(9):3280-8.
27. Moore LS, Rosenthal EL, de Boer E, Prince AC, Patel N, Richman JM, et al. Effects of an Unlabeled Loading Dose on Tumor-Specific Uptake of a Fluorescently Labeled Antibody for Optical Surgical Navigation. *Mol Imaging Biol.* 2017;19(4):610-6.
28. Davis SC, Samkoe KS, Tichauer KM, Sexton KJ, Gunn JR, Deharvengt SJ, et al. Dynamic dual-tracer MRI-guided fluorescence tomography to quantify receptor density in vivo. *Proc Natl Acad Sci U S A.* 2013;110(22):9025-30.
29. Tichauer KM, Samkoe KS, Sexton KJ, Gunn JR, Hasan T, Pogue BW. Improved tumor contrast achieved by single time point dual-reporter fluorescence imaging. *J Biomed Opt.* 2012;17(6):066001.
30. Lu G, Nishio N, van den Berg NS, Martin BA, Fakurnejad S, van Keulen S, et al. Co-administered antibody improves penetration of antibody-dye conjugate into human cancers with implications for antibody-drug conjugates. *Nat Commun.* 2020;11(1):5667.
31. Samkoe KS, Tichauer KM, Gunn JR, Wells WA, Hasan T, Pogue BW. Quantitative in vivo immunohistochemistry of epidermal growth factor receptor using a receptor concentration imaging approach. *Cancer Res.* 2014;74(24):7465-74.
32. Tichauer KM, Samkoe KS, Sexton KJ, Hextrum SK, Yang HH, Klubben WS, et al. In vivo quantification of tumor receptor binding potential with dual-reporter molecular imaging. *Mol Imaging Biol.* 2012;14(5):584-92.
33. Tichauer KM, Samkoe KS, Gunn JR, Kanick SC, Hoopes PJ, Barth RJ, et al. Microscopic lymph node tumor burden quantified by macroscopic dual-tracer molecular imaging. *Nat Med.* 2014;20(11):1348-53.
34. Tichauer KM, Deharvengt SJ, Samkoe KS, Gunn JR, Bosenberg MW, Turk MJ, et al. Tumor endothelial marker imaging in melanomas using dual-tracer fluorescence molecular imaging. *Mol Imaging Biol.* 2014;16(3):372-82.
35. Wang C, Xu X, Folaron M, Gunn JR, Hodge S, Chen EY, et al. Improved Discrimination of Tumors with Low and Heterogeneous EGFR Expression in Fluorescence-Guided Surgery Through Paired-Agent Protocols. *Mol Imaging Biol.* 2021.
36. Yin L, Cao Z, Wang K, Tian J, Yang X, Zhang J. A review of the application of machine learning in molecular imaging. *Ann Transl Med.* 2021;9(9):825.
37. Kumar V, Gu Y, Basu S, Berglund A, Eschrich SA, Schabath MB, et al. Radiomics: the process and the challenges. *Magn Reson Imaging.* 2012;30(9):1234-48.
38. Lambin P, Rios-Velazquez E, Leijenaar R, Carvalho S, van Stiphout RG, Granton P, et al. Radiomics: extracting more information from medical images using advanced feature analysis. *Eur J Cancer.* 2012;48(4):441-6.
39. Smith MT, Vermeulen R, Li G, Zhang L, Lan Q, Hubbard AE, et al. Use of 'Omic' technologies to study humans exposed to benzene. *Chem Biol Interact.* 2005;153-154:123-7.

40. Gillies RJ, Kinahan PE, Hricak H. Radiomics: Images Are More than Pictures, They Are Data. *Radiology*. 2016;278(2):563-77.
41. Hosny A, Parmar C, Quackenbush J, Schwartz LH, Aerts HJWL. Artificial intelligence in radiology. *Nat Rev Cancer*. 2018;18(8):500-10.
42. Aerts HJ, Velazquez ER, Leijenaar RT, Parmar C, Grossmann P, Carvalho S, et al. Decoding tumour phenotype by noninvasive imaging using a quantitative radiomics approach. *Nat Commun*. 2014;5:4006.
43. Vallières M, Freeman CR, Skamene SR, El Naqa I. A radiomics model from joint FDG-PET and MRI texture features for the prediction of lung metastases in soft-tissue sarcomas of the extremities. *Phys Med Biol*. 2015;60(14):5471-96.
44. Kolossváry M, Kellermayer M, Merkely B, Maurovich-Horvat P. Cardiac Computed Tomography Radiomics: A Comprehensive Review on Radiomic Techniques. *J Thorac Imaging*. 2018;33(1):26-34.
45. Streeter SS, Hunt B, Zuurbier RA, Wells WA, Paulsen KD, Pogue BW. Developing diagnostic assessment of breast lumpectomy tissues using radiomic and optical signatures. *Sci Rep*. 2021;11(1):21832.
46. Samkoe KS, Sardar HS, Gunn J, Feldwisch J, Linos K, Henderson E, et al. Measuring microdose ABY-029 fluorescence signal in a primary human soft-tissue sarcoma resection. *Proc SPIE Int Soc Opt Eng*. 2019;10862.
47. Resch-Genger U, Hoffmann K, Hoffmann A. Standardization of fluorescence measurements: criteria for the choice of suitable standards and approaches to fit-for-purpose calibration tools. *Ann N Y Acad Sci*. 2008;1130:35-43.
48. DeRose PC, Resch-Genger U. Recommendations for fluorescence instrument qualification: the new ASTM Standard Guide. *Anal Chem*. 2010;82(5):2129-33.
49. Elliott JT, Dsouza AV, Davis SC, Olson JD, Paulsen KD, Roberts DW, et al. Review of fluorescence guided surgery visualization and overlay techniques. *Biomed Opt Express*. 2015;6(10):3765-82.
50. Sun R, Cuthbert H, Watts C. Fluorescence-Guided Surgery in the Surgical Treatment of Gliomas: Past, Present and Future. *Cancers (Basel)*. 2021;13(14).
51. Crawford KL, Pacheco FV, Lee YJ, Hom M, Rosenthal EL, Nguyen QT, et al. A Scoping Review of Ongoing Fluorescence-Guided Surgery Clinical Trials in Otolaryngology. *Laryngoscope*. 2022;132(1):36-44.
52. van Griethuysen JJM, Fedorov A, Parmar C, Hosny A, Aucoin N, Narayan V, et al. Computational Radiomics System to Decode the Radiographic Phenotype. *Cancer Res*. 2017;77(21):e104-e7.
53. Zwanenburg A, Vallières M, Abdalah MA, Aerts HJWL, Andrearczyk V, Apte A, et al. The Image Biomarker Standardization Initiative: Standardized Quantitative Radiomics for High-Throughput Image-based Phenotyping. *Radiology*. 2020;295(2):328-38.
54. Parmar C, Grossmann P, Bussink J, Lambin P, Aerts HJWL. Machine Learning methods for Quantitative Radiomic Biomarkers. *Sci Rep*. 2015;5:13087.

55. Fornacon-Wood I, Mistry H, Ackermann CJ, Blackhall F, McPartlin A, Faivre-Finn C, et al. Reliability and prognostic value of radiomic features are highly dependent on choice of feature extraction platform. *Eur Radiol.* 2020;30(11):6241-50.
56. Mayerhoefer ME, Materka A, Langs G, Häggström I, Szczypiński P, Gibbs P, et al. Introduction to Radiomics. *J Nucl Med.* 2020;61(4):488-95.
57. Liu Z, Wang S, Dong D, Wei J, Fang C, Zhou X, et al. The Applications of Radiomics in Precision Diagnosis and Treatment of Oncology: Opportunities and Challenges. *Theranostics.* 2019;9(5):1303-22.
58. Wong AJ, Kanwar A, Mohamed AS, Fuller CD. Radiomics in head and neck cancer: from exploration to application. *Transl Cancer Res.* 2016;5(4):371-82.
59. Leijenaar RT, Carvalho S, Hoebbers FJ, Aerts HJ, van Elmpt WJ, Huang SH, et al. External validation of a prognostic CT-based radiomic signature in oropharyngeal squamous cell carcinoma. *Acta Oncol.* 2015;54(9):1423-9.
60. Moon SH, Kim J, Joung JG, Cha H, Park WY, Ahn JS, et al. Correlations between metabolic texture features, genetic heterogeneity, and mutation burden in patients with lung cancer. *Eur J Nucl Med Mol Imaging.* 2019;46(2):446-54.
61. Choi ER, Lee HY, Jeong JY, Choi YL, Kim J, Bae J, et al. Quantitative image variables reflect the intratumoral pathologic heterogeneity of lung adenocarcinoma. *Oncotarget.* 2016;7(41):67302-13.
62. Sala E, Mema E, Himoto Y, Veeraraghavan H, Brenton JD, Snyder A, et al. Unravelling tumour heterogeneity using next-generation imaging: radiomics, radiogenomics, and habitat imaging. *Clin Radiol.* 2017;72(1):3-10.
63. Wesdorp NJ, Hellingman T, Jansma EP, van Waesberghe JTM, Boellaard R, Punt CJA, et al. Advanced analytics and artificial intelligence in gastrointestinal cancer: a systematic review of radiomics predicting response to treatment. *Eur J Nucl Med Mol Imaging.* 2021;48(6):1785-94.
64. HARALICK R, SHANMUGAM K, DINSTEN I. TEXTURAL FEATURES FOR IMAGE CLASSIFICATION. *Ieee Transactions on Systems Man and Cybernetics.* 1973;SMC3(6):610-21.
65. Jackson A, O'Connor JP, Parker GJ, Jayson GC. Imaging tumor vascular heterogeneity and angiogenesis using dynamic contrast-enhanced magnetic resonance imaging. *Clin Cancer Res.* 2007;13(12):3449-59.
66. Rose CJ, Mills SJ, O'Connor JP, Buonaccorsi GA, Roberts C, Watson Y, et al. Quantifying spatial heterogeneity in dynamic contrast-enhanced MRI parameter maps. *Magn Reson Med.* 2009;62(2):488-99.
67. Gibbs P, Turnbull LW. Textural analysis of contrast-enhanced MR images of the breast. *Magn Reson Med.* 2003;50(1):92-8.
68. van Keulen S, van den Berg NS, Nishio N, Birkeland A, Zhou Q, Lu G, et al. Rapid, non-invasive fluorescence margin assessment: Optical specimen mapping in oral squamous cell carcinoma. *Oral Oncol.* 2019;88:58-65.
69. van Keulen S, Nishio N, Birkeland A, Fakurnejad S, Martin B, Forouzanfar T, et al. The Sentinel Margin: Intraoperative *Ex Vivo* Specimen Mapping Using Relative Fluorescence Intensity. *Clin Cancer Res.* 2019;25(15):4656-62.

70. Sardar HS, Zai Q, Xu X, Gunn JR, Pogue BW, Paulsen KD, et al. Dual-agent fluorescent labeling of soft-tissue sarcomas improves the contrast based upon targeting both interstitial and cellular components of the tumor milieu. *J Surg Oncol.* 2020;122(8):1711-20.
71. Fakurnejad S, Krishnan G, van Keulen S, Nishio N, Birkeland AC, Baik FM, et al. *Intraoperative Molecular Imaging for ex vivo Assessment of Peripheral Margins in Oral Squamous Cell Carcinoma.* *Front Oncol.* 2019;9:1476.